Ionics (2023) 29:4825–4833
https://doi.org/10.1007/s11581-023-05159-9

RESEARCH

PdM (M = Fe, Co, Ni) bimetallic nanowires enhances oxygen reduction catalysis in acid medium

Dan Yu[1] · Seng Dong[2,3] · Qian Liu[1] · Weiyi Jia[2,3] · Faming Gao[1,4] · Yatao Wang[2,3]

Received: 9 June 2023 / Revised: 13 July 2023 / Accepted: 1 August 2023 / Published online: 17 August 2023

Abstract

The preparation of platinum-free electrocatalysts with ideal oxygen reduction reaction (ORR) activity is of great significance for cost-effective fuel cells. Herein, we synthesize a series of Pd-based (PdFe, PdCo, PdNi, and Pd) nanowires (PdM NWs). Their diameters are about 10 nm. And the lengths are up to even micrometers. The mass activity of the series of Pd-based catalysts followed the descending order: PdNi NWs/C > commercial Pt/C > PdCo NWs/C > PdFe NWs/C > pure Pd NWs/C. The optimal half-wave ($E_{1/2}$) of PdNi NWs/C (839 mV) is positive shift 138 and 25 mV compared with pure Pd NWs/C (701 mV) and commercial Pt/C (814 mV), respectively. The mass activity (MA) of PdNi NWs/C only dropped 28% after 10,000 potential cycles between 0.6 and 1.1 V versus RHE in acid medium. This work provides a promising and reliable strategy to synthesize high performance Pd-based electrocatalyst, which is promising alternative to expensive Pt-based electrocatalysts for fuel cells.

Keywords Bimetallic · Nanowires · Oxygen reduction reaction · Platinum-free electrocatalysts

Introduction

Proton exchange membrane fuel cells (PEMFCs), due to their high energy conversion efficiency, low operating temperature, and low pollution emissions, are important for energy equipment (such as renewable vehicles and portable electronic devices) in solving current energy crises [1–4]. The research of catalyst has mainly focused on Pt and Pt-based materials in the past long time due to the most effective performing of Pt in ORR [5–8]. However, the scarcity of resources and high price hinder the widespread use of Pt in fuel cells [9–13]. Recently, some non-precious catalysts or single atom-based catalysts are studied replace Pt [14–17]. The Pd element belongs to the same main group as the Pt element, which has similar characteristics with Pt in many aspects [18–23]. And the more abundant of Pd-based nanomaterials represent a class of prospective and available catalysts for ORR, which have equal or even superior electrocatalytic performances than Pt-based catalysts [24–26]. An interesting conclusion is reported that the ORR activity of Pd is strongly correlated with the morphology [22, 27]. The activity of one-dimensional (1D) Pd NWs is 10 times higher than that of Pd nanoparticles and has comparable activity to commercial Pt/C at fuel cell operating potential [28–31].

On the other hand, Pd and transition metal (M) alloyed catalysts (such as Co, Fe, or Ni) could change the Pd–Pd atomic distance and charge distribution, which make the catalyst surface species and form more active sites favoring ORR [2, 32–35]. Not only reduce the Pd loading but also significantly improve the catalytic activity of catalysts [36–39]. Hence, Pd-based bimetallic materials such as PdNi, PdCo, PdZn [40–42], and more complex components of catalysts such as Pd-skin/Pd_3Fe (111) and Pd-skin/PdCo were serviceable for ORR [43, 44], but still not widely used in acidic electrolytes. To this end, the fabrication of 1D PdM nanowires with ideal electrochemical performance in acidic electrolytes is highly necessary, yet

✉ Faming Gao
fmgao@tust.edu.cn

✉ Yatao Wang
wangyatao@kailuan.com.cn

1 Hebei Key Laboratory of Applied Chemistry, Yanshan University, Qinhuangdao 066004, China

2 Coal Chemical R&D Centr of Kailuan Group, Tangshan 063018, China

3 Hebei Provincial Technology Innovation Centre of Coal-Based Materials and Chemicals, Tangshan 063018, China

4 College of Chemical Engineering and Materials, Tianjin University of Science & Technology, Tianjin 300222, China

remains challenging. Pd-based nanowires, which has the characters of anisotropy and mechanical flexibility, with high activity and stability, are expected to replace traditional Pt-based catalysts and solve the problem of resource scarcity.

Taken together, we successfully prepare a series of PdM (M = Fe, Co, Ni) nanowires (PdM NWs) with respectable activity and stability for ORR in acid medium. The PdM NWs were prepared by a straightforward hydrothermal method [45]. Briefly, the PdM nanowires were prepared through the reaction of $PdCl_2$ and MCl_x aqueous solutions in 220 ℃ keep 160 min. Benefiting from the combination of morphological advantages and bifunctional group effects, the as-synthesized PdNi NWs was extraordinarily improved activity for ORR performance, and exhibited more positive half-wave potentials (839 mV) which compared with both pure Pd NWs (701 mV) and commercial Pt/C (814 mV) in acid mediun, respectively.

Experimental section

Materials

Nickel chloride ($NiCl_2$, 99.995%), iron chloride ($FeCl_3$), cobalt chloride ($CoCl_2$, 97%), palladium chloride ($PdCl_2$, Pd 59–60%), ascorbic acid (AA), and sodium iodide (NaI) were purchased from Aladdin. Poly (vinyl pyrrolidone) (PVP, mw = 1-1300000). Perchloric acid ($HClO_4$, 70%) 99.999% were purchased from Sigma-Aldrich. Commercial Pt/C catalyst (20% metal) were purchased from JM. Deionized (DI) water obtained from Wahaha was used in all our experiments. All materials were obtained from commercial suppliers and used without further purification.

Synthesis of the PdNi NWs

$PdCl_2$ (17.7 mg), $NiCl_2$ (10.7 mg), PVP (1000 mg, mW = 1-1300000), NaI (300 mg), and AA (45 mg) are added to a beaker containing 20 mL of water under ultrasonically for 30 min, and then transferred to a reaction vessel containing a Teflon-lined reactor. Reaction at 210 ℃ keeps 160 min and spontaneous cooling to room temperature. The black product is obtained by ethanol/acetone, and centrifuged 2–3 times at 9000 rmp to obtain PdNi NWs. The PdFe and PdCo NWs replace $NiCl_2$ with $FeCl_3$ and $CoCl_2$, and then are prepared in the same way. Removal of AA and the second metal precursor to synthesize the pure Pd NWs in the same condition.

Characterization

The morphology of Pd-based catalyst analyzes using transmission electron microscopy (TEM) (HITACHI HT7700 at an accelerating voltage of 120 kV). The elements are attached to the transmission microscope by an energy dispersive X-ray detection content and a proportional spectrometer (EDX) analyzer. X-ray diffraction (XRD) patterns are recorded at Rigaku D/MAX-2500 powder diffractometer with Cu-Kα X-ray source between 10 and 100 degrees (~ 2θ) at the speed of 4°/min. The compositions of the catalysts are measured by inductively coupled plasma atomic mass spectrometer (ICP-AES) (710-ES, Varian). The X-ray photoelectron spectroscopic (XPS) spectral conducts using a Thermo Scientific ESCALAB 250Xi photoelectron spectrometer with a Mg-Kα as the exciting source (1253.6 eV). High-resolution TEM (HRTEM), high-angle annular dark-field scanning transmission electron microscopy (HAADF-STEM), and energy dispersive X-ray spectroscopy (STEM-EDS) mapping are carried out on JEOL (JEM 2100 plus and JEM-F200).

Electrochemical measurement

Electrochemical performance test is performed at 25 ℃ using CHI 760 electrochemical analyzer (CH Instruments, Chenhua Co., Shanghai, China). A common three-electrode system, Pt plate as the counter electrode, 3.5 M Ag/AgCl as the reference electrode, and the working electrode is a rotating disk electrode (RDE) with a working area of 0.196 cm^2 with a diameter of 5 mm. Various Pd-based nanowires are mixed with XC-72 C to prepare catalyst powders with a metal content of about 20%. The previously prepared catalyst powder is dissolved in a mixed solution of isopropyl alcohol/water with 0.5% of Nafion to preparing a mixture of 1 mg $_{(catalyst)}$/mL, and ultrasonic for 30 min to obtain a well-proportioned ink. The rotating disk electrode (RDE) is polished with alumina powder and ultrasonically cleaned. A total of 10 uL of the catalyst ink is applied to the surface of the electrode to have a catalyst loading of 10 ug cm^{-2}. The catalyst layer was dried at 25 ℃ for electrochemical testing.

Results and discussions

As Fig. 1 shows, there are three major steps to synthesize PdM NWs. First, the mix solution of $PdCl_2$, MCl_x, NaI, AA, and PVP is ultrasonic treatment for 30 min until dissolve completely. Then, the uniform dark red mixed solution is

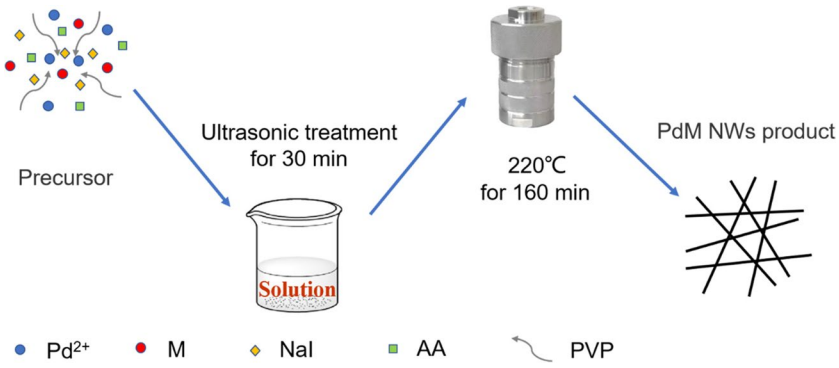

Fig. 1 Schematic illustration of forming PdM (M = Fe, Co, Ni) NWs

transferred to hydrothermal reactor, which is heated at 200 ℃ for 160 min. Finally, the PdM NWs is obtained by centrifugal separation.

The morphology and structure of the PdM NWs take using transmission electron microscope (TEM), high resolution transmission electron microscopy (HRTEM), high-angle annular dark-field scanning TEM (HAADF-STEM), X-ray photoelectron spectroscopy (XPS), and X-ray diffraction (XRD). Using PdNi NWs as an example, the TEM image is shown in Fig. 2a. The length of the PdNi NWs is several microns and the distribution is extraordinary even. Figure 2b and c show the highly megascopic TEM image; the diameter of the PdNi NWs is approximately 10 nm, which has smooth surface and uniform thickness. The diameter of the PdNi nanowire is slightly larger than that of the pure Pd nanowire (about 6 nm, Figure S1), which considered to be affected by the second metal doping. As shown in Fig. 2d (the HRTEM image is obtained from the blue box in Fig. 2c), the lattice fringes are clearly visible. The interplanar spacing displays 0.193 nm and 0.223 nm slightly lower than that of the (200) and (111) plane of fcc Pd, revealing the formation of PdNi NWs, which in line with the result of XRD (Figure S2).

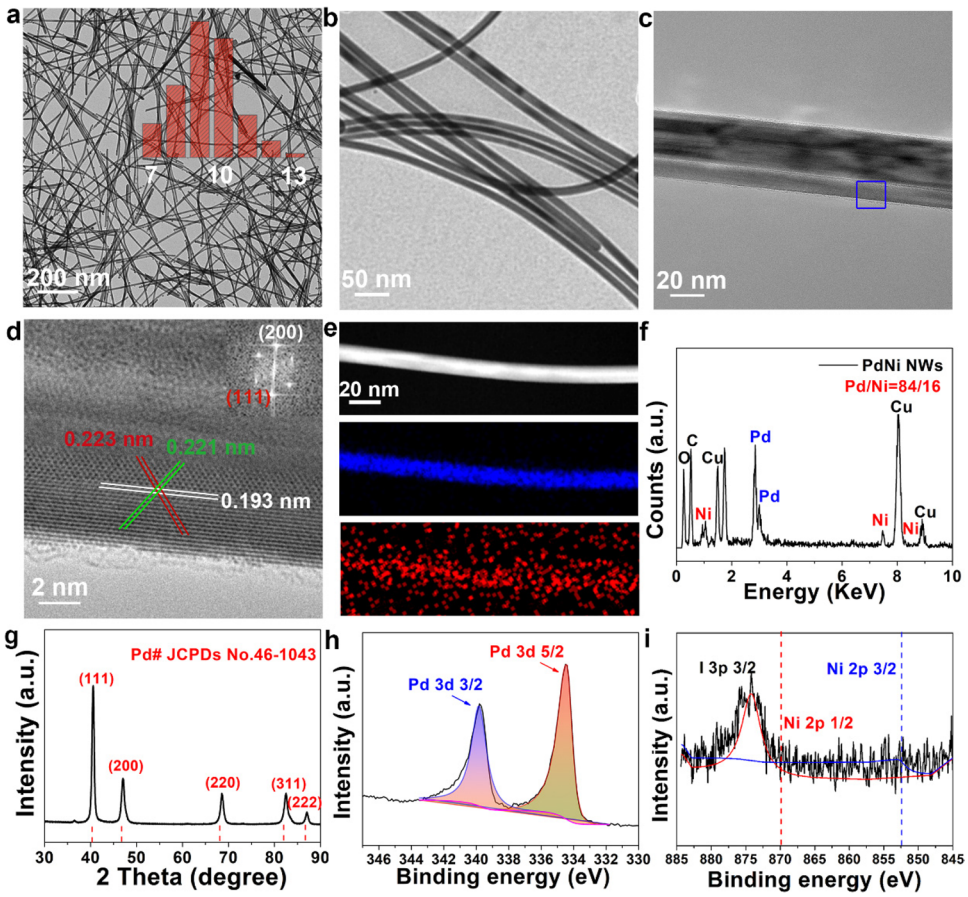

Fig. 2 Structural and compositional analysis of PdNi NWs. **a** Low- and **b** and **c** high-magnification TEM images, inset in **a** is diameter histogram of PdNi NWs. **d** HRTEM image projected along the zone axes of [110] axis. The inset is FFT pattern. **e** STEM-EDS elemental mapping images of Pd and Ni. **f** TEM-EDS spectrum. **g** XRD pattern. **h** XPS spectra of Pd 3d and **i** Ni 2p

The fast Fourier transform (FFT) pattern is shown inset of Fig. 2d. Figure 2e shows the STEM energy-dispersive X-ray spectroscopy (STEM-DES) elemental mapping images of PdNi NWs, which indicates the homogeneous distribution of Pd and Ni the NWs. Figure 2f shows the TEM-EDS, the atomic percent of Pd and Ni in NWs is confirmed to 84/16, which agrees with the result from inductively coupled plasma-atomic emission spectroscopy (ICP-AES, 84.6/15.4, shown in Table S2). A typic face-centered cubic (fcc) crystal phase is verified by XRD (Fig. 2g). All the characteristic diffraction peaks of PdNi NWs are positive shift to higher diffraction angle compared to Pd (JCPDS No. 46–1043), confirming a lattice contraction due to the formation of PdNi NWs [41, 42]. The XPS spectra of PdNi NWs illustrate the presence of Pd and Ni of PdNi NWs. Figure 2h shows the Pd 3d spectrum, with the Pd 3d 3/2 and Pd 3d 3/2 peak at 339.8 eV and 334.5 eV, respectively. Figure 2i shows the Ni 2p spectrum, the peak of transition element is not obvious in XPS, we think these may be due to the magnetic properties of the element and the surface content of the PdNi NWs.

The present synthetic method is also suitable for the preparation of different types of PdM NWs, including PdCo and PdFe. The XRD pattern in Figure S2 shows that all the PdM NWs in this work (Pd, PdFe, PdCo, PdNi) can be assigned fcc crystal phase. The average width of PdFe NWs is 10 nm, and length up to microns (Fig. 3a). Figure 3b_1–b_3 show the STEM-DES elemental mapping images of PdFe NWs, indicating the homogeneous distribution of Pd and Fe in the NWs. The HRTEM image of PdFe NWs exhibits the lattice spacing of 0.223 nm (Fig. 3b_4), determining to the (111) plane of fcc Pd. TEM-EDS estimates that the composition ratio of Pd/Fe is 83/17 (Fig. 3c). By replacing the $CoCl_2$ with $FeCl_3$, the PdCo NWs with semblable structure and morphology is made. Figure 3d shows the TEM image of PdCo NWs, which has similar morphology to PdFe NWs. Figure 3e_1–e_3 show the STEM-DES elemental mapping images of PdCo NWs. The lattice spacing of 0.222 nm of PdCo NWs is obtained from HRTEM image (Fig. 3e_4). Figure 3f shows the TEM-EDS. For comparison, the Pd NWs is also prepared in the same condition, which except dropping AA and MCl_x. Figure S1 shows the average width of 6 nm and length of several micron of Pd NWs. The lattice spacing of 0.198 nm can be assigned to (111) plane (Figure S1c). The XRD pattern (Figure S2) of Pd NWs can match well with the peaks of Pd material (JCPDS No. 46–1043). Figure S1d shows the TEM-EDS spectrum of Pd NWs.

To investigate the ORR performance, the PdFe NWs, PdCo NWs, PdNi NWs, and Pd NWs are loaded onto commercial carbon (C, Vulcan XC-72) and then under magnetic stirring overnight. Washing the mixture with water/ethanol 5 times to remove excess surfactant and ionic species, and then anneal at 200 ℃ for 80 min to obtain

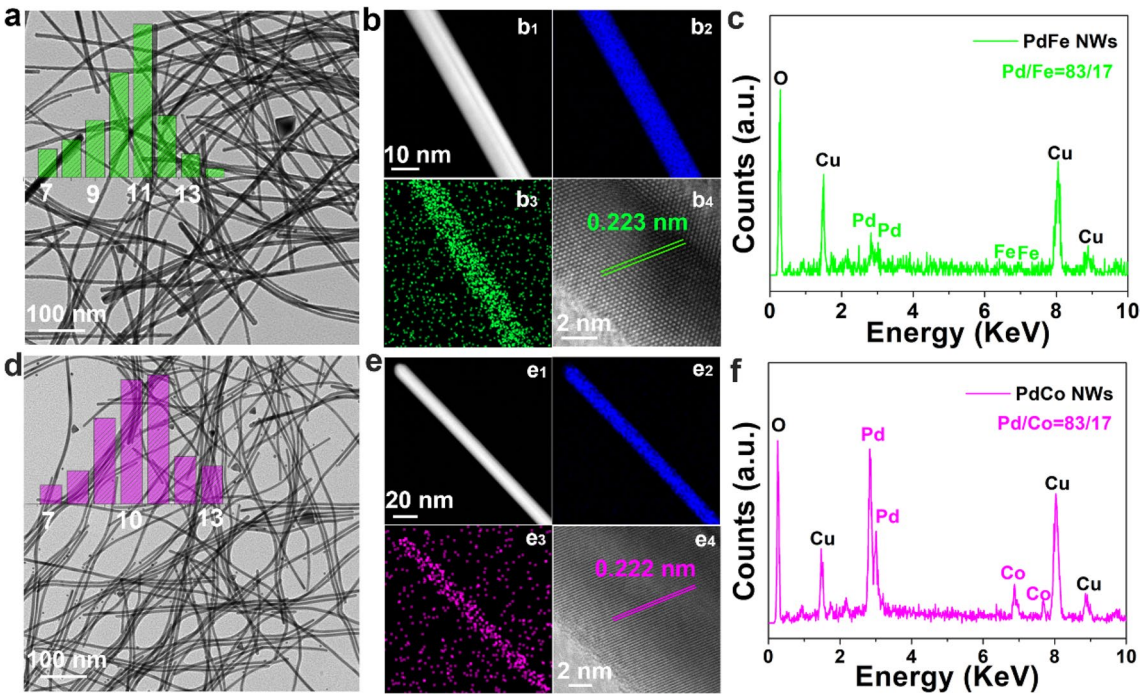

Fig. 3 Structural and compositional analysis of PdFe and PdCo NWs. **a** TEM image, inset is diameter histogram of PdFe NWs. **b_1–b_3** STEM-EDS elemental mapping images of Pd and Fe. **b_4** HRTEM image. **c** TEM-EDS spectrum of PdFe NWs. **d** TEM image, inset is diameter histogram of PdCo NWs. **e_1–e_3** STEM-EDS elemental mapping images of Pd and Co. **e_4** HRTEM image. **f** TEM-EDS spectrum of PdCo NWs

the catalyst with clean surface. The resulting electrocatalysts are PdFe NWs/C, PdCo NWs/C, and PdNi NWs/C electrocatalysts for ORR, which compares with pure Pd NWs/C and commercial Pt/C. The electrochemical performance of the series of catalysts is performed with the rotating disk electrode (RDE) method. Before the electrochemical measurements, the electrocatalyst is activated in N_2-sturated 0.1 M $HClO_4$ for 500 cycles at a sweep rate of 500 mV S^{-1} between 0.05 and 1.1 V versus reversible hydrogen electrode (RHE). Cyclic voltammograms (CVs) of different catalysts are shown in Figure S3. Considering that Pd is accompanied by the absorption of H in the hydrogen desorption charge ($H^+ + e^- = H_{upd}$) process, the H_{upd} method cannot be used to calculate electrochemical active surface area (ECSA) of Pd-based materials. We depict the ECSA values of PdM NWs/C by the following equation:

$$ECSA = \frac{Q}{mC}$$

where Q is the charges involves with the reduction region of PdO and m is the mass of Pd loading on the surface of glassy carbon electrode (GCE). C is assumed to be 0.424 mC cm^{-2}, which represents for the electrical charge constant associated with the reduction of PdO monolayer [22, 46, 47]. Although this assumption may generate some uncertainties, it is acceptable when the content of the second metal (M) in the catalyst is much lower than that of Pd (the proportion of M to total mass is less than 25%) [41]. According to the CVs, the ECSA of the series of PdM NWs/C exceed to be greater than Pd NWs/C (Figure S4), indicating that such PdM NWs/C catalysts possessed more electro-chemically active sites than pure Pd NWs/C.

The ORR polarization curves of the series of catalysts are collected with RDE in an O_2-saturated 0.1 M $HClO_4$ solution under a rotating rate of 1600 rpm. Two distinguishable potential ranges in Fig. 4a are the diffusion-controlled range below 0.7 V with a diffusion limited current density 5–6 mA cm^{-2} and the mixed kinetic/diffusion-controlled range of 0.7–1.0 V. The half-wave potential ($E_{1/2}$) of each catalyst is summarized in Fig. 4b: PdNi NWs/C (0.839 V) > PdFe NWs/C (0.821 V) > commercial Pt/C (0.814 V) > PdCo NWs/C (0.774 V) > pure Pd NWs/C (0.701 V), indicating conspicuously enhanced ORR activity of PdNi NWs/C and has a smaller overpotential than pure Pd NWs/C or commercial Pt/C. Likewise, the corresponding mass activity (MA) of different PdM NWs/C catalysts at 0.9 V vs. RHE is shown in Fig. 4c. The MA of each catalyst follows the sequence of PdNi NWs/C (140 mA mg^{-1}) > commercial Pt/C (130 mA mg^{-1}) > PdFe NWs/C (102 mA mg^{-1}) > PdCo NWs/C (70 A mg^{-1}) > pure Pd NWs/C (16 A mg^{-1}). PdNi NWs/C exhibits the highest MA among all catalysts, which is 1.07 and 8.75 times higher than those of commercial Pt/C and pure Pd NWs/C. It shows that M doping in PdM NWs can significantly improve the ORR performance. Furthermore, the PdNi NWs/C exhibits highest kinetic current density among all studied catalysts in this work (Fig. 4d). And the comparison table of half-wave potential of recently reported palladium-based catalysts is shown in Table S3. Figure 4e shows the linear sweep voltammetry (LSV) polarization curves of PdNi NWs/C at rotating speeds

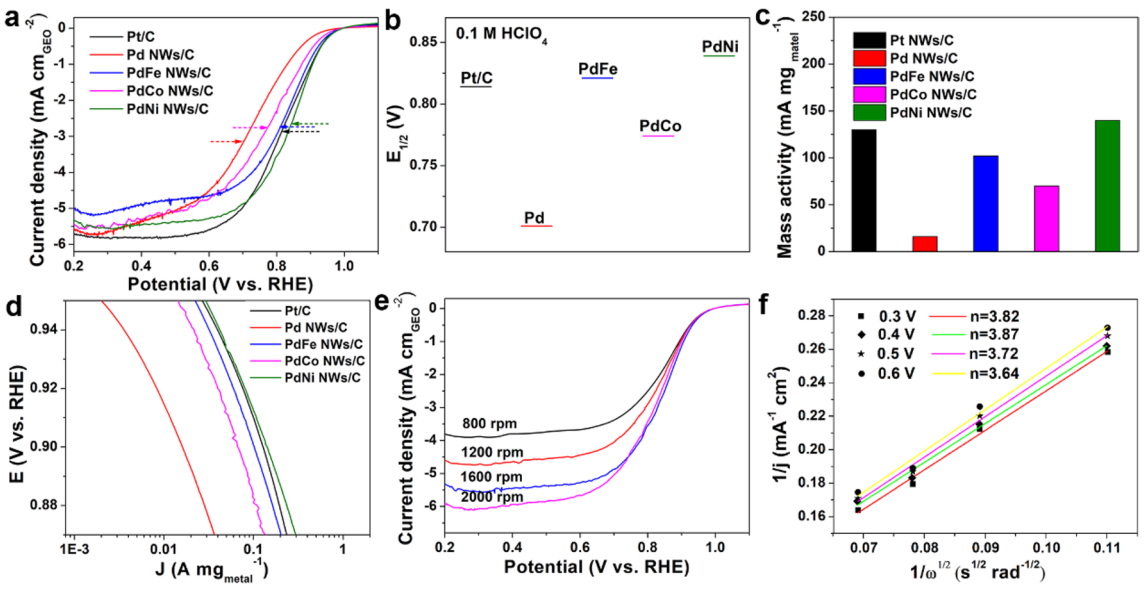

Fig. 4 ORR performance of PdM/C NWs, pure Pd NWs/C, and commercial Pt/C. **a** ORR polarization curves. **b** Comparison of half-wave for different catalysts. **c** Comparison of mass activity at 0.9 V. **d** Tafel plots. **e** Linear sweep voltammetry polarization curves at various rotation rates. **f** Koutecky-Levich plots of PdNi NWs/C at different potentials

ranging from 800 to 2000 rpm. The LSV curves in Fig. 4e reveal that diffusion-limiting current rises with the increasing rotation speeds. The mass-transport limited current density at a given rotation speed in turn, $j_{diffusion}$, is given by:

$$j_{diffusion} = xnFD^{2/3}v^{-1/6}C_{O_2}\omega^{1/2}$$

where ω is rotation speed, n is the number of transferred electrons, F is the Faraday constant, D is the diffusion coefficient, v is the kinetic viscosity, and C_{O_2} is the bulk concentration of O_2. Therefore, diffusion-limiting current $j_{diffusion}$ rises with the increasing rotation speeds ω. The Koutecky-Levich (K-L) plots obtained from Fig. 4e, as shown in Fig. 4f, which displays the nearly parallel fitting lines, revealing the electron transfer rate independent of potential and the first-order reaction kinetics for ORR related to O_2 concentration. The number of electron transfer is confirmed to be 3.64–3.82 in the potential region of 0.3–0.6 V vs. RHE, exhibiting a decent four-electron transfer pathway and a minimal peroxide formation. A comparison table of the current samples with reported Pd-based electrocatalysts in ORR activity is shown in Table S1. The excellent electrochemical performance of PdM NWs/C can be ascribed to the following aspects: (1) the unique morphology of 1 D nanowires provides a direct channel for electron transfer in the electrochemical reaction process, which is conducive to the ORR activity of materials. (2) The formation of PdNi alloy would be favorable to increase the d-band vacancy and reduce the d-band center (ligand effect), which enhance the ORR activity [48, 49]. (3) The strain effect of Pd and Ni shrink the lattice, weaking the excessive adsorption of Pd to O, and further enhance the ORR activity in view of its mechanism [2, 50].

Additionally, for an ideal ORR catalyst, the tolerance effect of small-molecule fuels is important; we further performed the methanol tolerance test in Figure S9. The chronoamperometric responses of the catalysts to the addition of 2 M methanol at 0.55 V versus RHE 0.1 M HClO4 solution were recorded. There was no obvious change in the current density on PdNi NWs/C catalyst electrode after injecting 2 M methanol into the electrolyte, indicating that PdNi NWs/C catalyst was nearly free from the methanol penetration effect.

The durability of different PdM NWs/C catalysts is evaluated by performing accelerated durability test

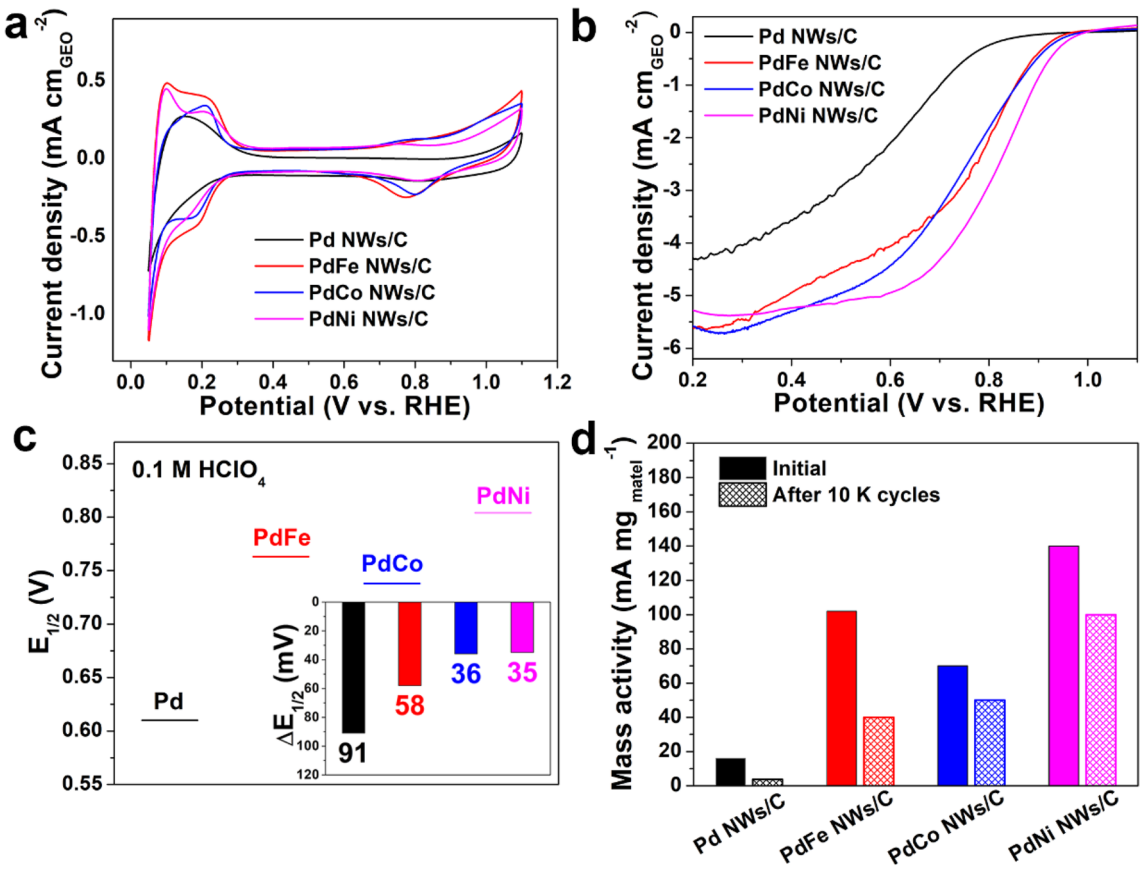

Fig. 5 Stability of different catalysts after 10,000 potential cycles between 0.6 and 1.1 V (RHE). **a** CVs. **b** ORR polarization curves. **c** Comparison of half-wave and **d** mass activity at 0.9 V

(ADT) in 0.1 M $HClO_4$ under a sweep rate of 200 mV s^{-1}, at the potential ranges of 0.6–1.1 V. The CVs of different PdM NWs/C catalysts after 10 000 cycles are shown in Fig. 5a, and the ECSAs of different PdM NWs/C catalysts are shown in Figure S5. The ORR polarization curves of different catalysts before and after 10,000 potential cycles are shown in Fig. 5b. The $E_{1/2}$ of PdNi NWs/C exhibits 35 mV negative shift ($\Delta E_{1/2}$), in contrast to that of PdCo NWs/C (36 mV), PdFe NWs/C (58 mV), and Pd NWs/C (91 mV), as displayed in Fig. 5c and table S3. Especially, the overpotential of PdNi NWs/C at − 3 mA cm^{-2} increased from 372 to 406 mV after 10,000 potential cycles (Figure S6). The PdNi NWs/C still afford MA of 101 mA mg^{-1} at 0.9 V after 10,000 potential cycles, dropping only 28% compared with initial value. By comparison, the PdCo NWs/C, PdFe NWs/C, and Pd NWs/C drop 29%, 61%, and 77% of their initial value (Fig. 5d). We performed TEM tests on the samples before and 10,000 potential cycles (Figure S7). Obviously, the results show that the morphology of PdNi NWs/C is the most complete after accelerated durability test. The smooth surface of PdNi NWs/C becomes rough, but the overall 1D structure is almost no change, which is probably caused by the dissolution of Ni on the nanowire surface during operation in acidic medium. In contrast, the morphologies of PdCo NWs/C and PdFe NWs/C have changed dramatically. The acid corrosion degree and location of different catalysts are different, indicating that their active sites may be different. We also performed the chronoamperometry test at 0.55 V in Figure S10. The current density for sample PdNi NWs/C loses 39% of its original current density after 5 h holding test. However, commercial Pt/C loses 69% of its original current density. This result indicates that PdNi NWs/C shows higher stability than Pt/C. The preferable durability of PdM NWs/C can be attributed to its unique morphology: (1) the anisotropy of the 1D nanostructure can effectively reduce the activity reduction caused by the agglomeration and accumulation of the catalyst. The size of the nanoparticles increased significantly after 10,000 potential cycles, indicating the nanoparticles tend to agglomerate (Figure S8b, d). (2) The excellent mechanical toughness of 1D nanowires can inhibit mechanical degradation during the ORR process and extend the cycle life of the catalysts.

Conclusion

In summary, we synthesized a series of PdM 1D nanostructure using a simple hydrothermal method, improving the ORR performance of Pd-based nanowires by doping Fe, Co, or Ni. The length of the Pd-based nanowires is several microns and the diameter is approximately 10 nm. Hereinto, the $E_{1/2}$ of PdNi NWs/C exhibits (0.839 V) is positive shift 25 mV and 138 mV than commercial Pt/C (0.814 V) and pure Pd NWs/C (0.701 V) in acid medium. The PdM NWs/C shows better stability than pure Pd NWs/C after 10,000 potential cycles. We anticipate that this research will inspire the rational design of the usable high-efficiency platinum free catalysts, and widely used in the field of cost-effective fuel cells.

Supplementary Information The online version contains supplementary material available at https://doi.org/10.1007/s11581-023-05159-9.

Author contribution DY, FG, and YW: conceptualization. DY, SD, QL, and WJ: methodology and investigation. DY and FG: writing—original draft. FG and YW: writing—review and editing.

Funding The financial support from the National Natural Science Foundation of China (Grant No. 21875205) and the Natural Science Foundation of Hebei (Grant No. 22281403Z and B2021203016).

Data availability Not applicable.

Declarations

Ethical approval Not applicable.

Competing interests The authors declare no competing interests.

References

1. Xu H, Shang H, Wang C, Du Y (2020) Ultrafine Pt-based nanowires for advanced catalysis. Adv Func Mater 30:2000793
2. Zhang L, Chang Q, Chen H, Shao M (2016) Recent advances in palladium-based electrocatalysts for fuel cell reactions and hydrogen evolution reaction. Nano Energy 29:198–219
3. Luo M, Sun Y, Zhang X, Qin Y, Li M, Li Y, Li C, Yang Y, Wang L, Gao P, Lu G, Guo S (2018) Stable high-index faceted Pt skin on zigzag-like PtFe nanowires enhances oxygen reduction catalysis. Adv Mater 30:1705515
4. Shang C, Guo Y, Wang E (2018) Facile fabrication of PdRuPt nanowire networks with tunable compositions as efficient methanol electrooxidation catalysts. Nano Res 11:4348–4355
5. Tao L, Huang B, Jin F, Yang Y, Luo M, Sun M, Liu Q, Gao F, Guo S (2020) Atomic PdAu interlayer sandwiched into Pd/Pt core/shell nanowires achieves superstable oxygen reduction catalysis. ACS Nano 14:11570–11578
6. Chao T, Zhang Y, Hu Y, Zheng X, Qu Y, Xu Q, Hong X (2020) Atomically dispersed Pt on screw-like Pd/Au core-shell nanowires for enhanced electrocatalysis. Chemistry 26(18):4019–4024
7. Shao Q, Lu K, Huang X (2019) Platinum group nanowires for efficient electrocatalysis. Small Methods 3:1800545
8. Wang L, Holewinski A, Wang C (2018) Prospects of platinum-based nanostructures for the electrocatalytic reduction of oxygen. ACS Catal 8:9388–9398
9. Renzi M, Nobili F, Miecznikowski K, Kostuch A, Wadas A, Rutkowska IA, Kulesza PJ (2022) Activation of bimetallic PtFe nanoparticles with zeolite-type cesium salts of vanadium-substituted

polyoxometallates toward electroreduction of oxygen at low Pt loadings for fuel cells. J Solid State Electrochem 26(1):3–16
10. Yu D, Feng Y, Jin J, Liu Q, Tao L, Zhou J, Hou L, Gao F (2021) Bimetallic PdPt with Pt-Shell porous nanotubes for efficient oxygen reduction electrocatalysis. Microporous Mesoporous Mater 323:111188
11. Matin MA, Lee J, Kim GW, Park H-U, Cha BJ, Shastri S, Kim G, Kim Y-D, Kwon Y-U, Petkov V (2020) Morphing Mncore@ Ptshell nanoparticles: effects of core structure on the ORR performance of Pt shell. Appl Catal B: Environ 267:118727
12. Zhu X, Tan X, Wu K-H, Haw S-C, Pao C-W, Su B-J, Jiang J, Smith SC, Chen J-M, Amal R, Lu X (2021) Intrinsic ORR activity enhancement of Pt atomic sites by engineering the d-band center via local coordination tuning. Angew Chem 60:21911–21917
13. Shen H, Gracia-Espino E, Ma J, Zang K, Luo J, Wang L, Gao S, Mamat X, Hu G, Wagberg T, Guo S (2017) Synergistic effects between atomically dispersed Fe-N-C and C-S-C for the oxygen reduction reaction in acidic media. Angew Chem 56:13800–13804
14. Wolker T, Brunnengräber K, Martinaiou I, Lorenz N, Zhang G-R, Kramm UI, Etzold BJM (2022) The effect of temperature on ionic liquid modified Fe-N-C catalysts for alkaline oxygen reduction reaction. J Energy Chem 68:324–329
15. Zhao C-X, Ren D, Wang J, Liu J-N, Tang C, Chen X, Li B-Q, Zhang Q (2022) Regeneration of single-atom catalysts deactivated under acid oxygen reduction reaction conditions. J Energy Chem 73:478–484
16. Liu Y, He SQ, Huang B, Kong ZY, Guan LH (2022) Influence of different Fe doping strategies on modulating active sites and oxygen reduction reaction performance of Fe, N-doped carbonaceous catalysts. J Energy Chem 70:511–520
17. Zhao X, Chen J, Bi Z, Chen S, Feng L, Zhou X, Zhang H, Zhou Y, Wågberg T, Hu G (2023) Electron modulation and morphology engineering jointly accelerate oxygen reaction to enhance Zn-Air battery performance. Adv Sci 10:2205889
18. Zhan Y, Huang B, Luo G, Sun T, Feng YG, Wang YH, Ma YH, Shao Q, Li YF, Zhou ZY, Huang XQ (2020) Atomically deviated Pd-Te nanoplates boost methanol-tolerant fuel cells. Sci Adv 6:9731
19. Li W, Haldar P (2009) Supportless PdFe nanorods as highly active electrocatalyst for proton exchange membrane fuel cell. Electrochem Commun 11:1195–1198
20. Wang J, Kong H, Zhong H, Jiang Y, Guo F, Alonso-Vante N, Feng Y (2021) Recent progress on transition metal based layered double hydroxides tailored for oxygen electrode reactions. Catalysts 11:1394
21. Wang X, Ma G, Zhu F, Lin N, Tang B, Zhang Z (2013) Preparation and characterization of micro-arc-induced Pd/TM(TM=Ni, Co and Ti) catalysts and comparison of their electrocatalytic activities toward ethanol oxidation. Electrochim Acta 114:500–508
22. Zhang K, Xu H, Yan B, Wang J, Du Y, Liu Q (2018) Superior ethylene glycol oxidation electrocatalysis enabled by hollow PdNi nanospheres. Electrochim Acta 268:383–391
23. Chen L, Guo H, Fujita T, Hirata A, Zhang W, Inoue A, Chen M (2011) Nanoporous PdNi bimetallic catalyst with enhanced electrocatalytic performances for electro-oxidation and oxygen reduction reactions. Adv Func Mater 21:4364–4370
24. Zhang LY, Zeng TT, Zheng LW, Wang YR, Yuan WY, Niu M, Guo CX, Cao DP, Li CM (2023) Epitaxial growth of Pt–Pd bimetallic heterostructures for the oxygen reduction reaction. Adv Powder Mater 2:100131
25. Zeng TT, Zheng LW, Chen HB, Wang YR, Ling M, Sun SW, Zhang F, Yuan WY, Zhang LY (2023) One-pot controllable epitaxial growth of Pd-based heterostructures for enhanced formic acid oxidation. Colloids Surf A 656:130358
26. Zeng TT, Meng XM, Huang HW, Zheng LW, Chen HB, Zhang Y, Yuan WY, Zhang LY (2022) Controllable synthesis of web-footed PdCu nanosheets and their electrocatalytic applications. Small 18:2107623
27. Zuo Y, Rao D, Li S, Li T, Zhu G, Chen S, Song L, Chai Y, Han H (2018) Atomic vacancies control of Pd-based catalysts for enhanced electrochemical performance. Adv Mater 30:1704171
28. Jiang X, Xiong Y, Zhao R, Zhou J, Lee J-M, Tang Y (2020) Trimetallic Au@PdPb nanowires for oxygen reduction reaction. Nano Res 13:2691–2696
29. Kottayintavida R, Gopalan NK (2020) Pd modified Ni nanowire as an efficient electro-catalyst for alcohol oxidation reaction. Int J Hydrogen Energy 45:8396–8404
30. Zhang Y-L, Sui X-L, Zhao L, Gu D-M, Huang G-S, Wang Z-B (2019) Controlling the surface roughness of chain-like Pd nanowires by pH values as excellent catalysts for oxygen reduction reaction. Int J Hydrogen Energy 44:6551–6559
31. Xue Q, Bai J, Han C, Chen P, Jiang J-X, Chen Y (2018) Au nanowires@Pd-polyethylenimine nanohybrids as highly active and methanol-tolerant electrocatalysts toward oxygen reduction reaction in alkaline media. ACS Catal 8:11287–11295
32. Martins M, Metin Ö, Šljukić B, Sevim M, Sequeira C, Santos D (2019) PdNi alloy nanoparticles assembled on cobalt ferrite-carbon black composite as a fuel cell catalyst. Int J Hydrogen Energy 44:14193–14200
33. Zhu H, Luo M, Zhang S, Wei L, Wang F, Wang Z, Wei Y, Han K (2013) Combined method to prepare core–shell structured catalyst for proton exchange membrane fuel cells. Int J Hydrogen Energy 38:3323–3329
34. Šljukić B, Martins M, Kayhan E, Balčiūnaitė A, Şener T, Sequeira CAC, Santos DMF (2017) SnO 2 -C supported PdNi nanoparticles for oxygen reduction and borohydride oxidation. J Electroanal Chem 797:23–30
35. Holade Y, da Silva RG, Servat K, Napporn TW, Canaff C, de Andrade AR, Kokoh KB (2016) Facile synthesis of highly active and durable PdM/C (M = Fe, Mn) nanocatalysts for the oxygen reduction reaction in an alkaline medium. J Mater Chem A 4:8337–8349
36. Chen T-W, Kang J-X, Zhang D-F, Guo L (2016) Ultralong PtNi alloy nanowires enabled by the coordination effect with superior ORR durability. RSC Adv 6:71501–71506
37. Li X, Li X, Liu C, Huang H, Gao P, Ahmad F, Luo L, Ye Y, Geng Z, Wang G, Si R, Ma C, Yang J, Zeng J (2020) Atomic-level construction of tensile-strained PdFe alloy surface toward highly efficient oxygen reduction electrocatalysis. Nano Lett 20:1403–1409
38. Yang J, Zhou W, Cheng CH, Lee JY, Liu Z (2010) Pt-decorated PdFe nanoparticles as methanol-tolerant oxygen reduction electrocatalyst. ACS Appl Mater Interfaces 2:119–126
39. Xu C, Liu Y, Zhang H, Geng H (2013) A nanoporous PdCo alloy as a highly active electrocatalyst for the oxygen-reduction reaction and formic acid electrooxidation. Chem Asian J 8:2721–2728
40. Kim D-S, Kim J-H, Jeong I-K, Choi JK, Kim Y-T (2012) Phase change of bimetallic PdCo electrocatalysts caused by different heat-treatment temperatures: effect on oxygen reduction reaction activity. J Catal 290:65–78
41. Bampos G, Bebelis S, Kondarides DI, Verykios X (2017) Comparison of the activity of Pd–M (M: Ag Co, Cu, Fe, Ni, Zn) bimetallic electrocatalysts for oxygen reduction reaction. Top Catal 60:1260–1273
42. Yang Y, Xiao W, Feng X, Xiong Y, Gong M, Shen T, Lu Y, Abruna HD, Wang D (2019) Golden palladium zinc ordered intermetallics as oxygen reduction electrocatalysts. ACS Nano 13:5968–5974
43. Son DN, Thanh PN, Quang ND, Takahashi K, Pham-Ho MP (2017) First-principles study of Pd-skin/Pd3Fe(111)

electrocatalyst for oxygen reduction reaction. J Appl Electrochem 47:747–754
44. Son DN, Le OK, Chihaia V, Takahashi K (2015) Effects of Co content in Pd-skin/PdCo alloys for oxygen reduction reaction: density functional theory predictions. J Phys Chem C 119:24364–24372
45. Zheng NF, Huang XQ (2009) One-pot, high-yield synthesis of 5-fold twinned Pd nanowires and nanorods. J Am Chem Soc 131:4602–4603
46. Liu Z, Yang X, Cui L, Shi Z, Lu B, Guo X, Zhang J, Xu L, Tang Y, Xiang Y (2018) High-performance oxygen reduction electrocatalysis enabled by 3D PdNi nanocorals with hierarchical porosity. Part Part Syst Charact 35:1700366
47. Chierchie T, Mayer C, Lorenz WJ (1982) Structural changes of surface oxide layers on palladium. J Electroanal Chem Interfacial Electrochem 135:211–220
48. Greeley J, Stephens IE, Bondarenko AS, Johansson TP, Hansen HA, Jaramillo TF, Rossmeisl J, Chorkendorff I, Norskov JK (2009) Alloys of platinum and early transition metals as oxygen reduction electrocatalysts. Nat Chem 1:552–556
49. Hao L, Kihyun S, Graeme H (2018) Effects of ensembles, ligand, and strain on adsorbate binding to alloy surfaces. J Chem Phys 149:174705
50. Mavrikakis M, Hammer B, Nørskov JK (1998) Effect of strain on the reactivity of metal surfaces. Phys Rev Lett 81:2819–2822